Unified Evaluation of Slope Displacement Using Energy-Based Newmark Method for Arbitrary Earthquake Motions

Takaji Kokusho *, Tomohiro Ishizawa , Jiro Mori , Michinori Mizuhara

Posted Date: 25 March 2026

doi: 10.20944/preprints202603.1883.v1

Keywords: seismic slope stability; sliding displacement; energy balance; earthquake wave energy; Newmark model; wave irregularity; infinite slope model; unified design diagram; arbitrary earthquakes

 doi:10.20944/preprints202603.1883.v1

Article

Unified Evaluation of Slope Displacement Using Energy-Based Newmark Method for Arbitrary Earthquake Motions

Takaji Kokusho [1,*], Tomohiro Ishizawa [2], Jiro Mori [3] and Michinori Mizuhara [3]

[1] Chuo University (Professor Emeritus), Tokyo, Japan
[2] National Research Institute for Earth Science and Disaster Resilience, Tsukuba, Japan
[3] West Jec. Inc. Fukuoka, Japan
* Correspondence: koktak@ad.email.ne.jp

Abstract

Slope displacements (δ) have been shown to correlate uniquely with the earthquake energy (E_{eq}) contributing to slope sliding, regardless of input motion characteristics. Based on this principle, this study applies the Energy-Based Newmark Method to infinitely long slopes subjected to diverse ten earthquake records with incrementally scaled amplitudes. As the earthquake wave energy (E_u) increases, the energy ratio (E_{eq}/E_u) exhibits a distinct peak followed by a monotonic decrease. These peak values and corresponding E_u levels strongly depend on the predominant frequencies (f_p) of the motions, consistent with results from harmonic wave analyses. A unified design diagram is developed to correlate E_{eq}/E_u with E_u incorporating f_p and slope parameters. Since both E_u and f_p can be estimated from design motions or empirically predicted using earthquake magnitude and source distance, the slope displacement δ can be directly obtained from the diagram, eliminating the need for time-domain numerical simulations used in the conventional Newmark approaches. This method is recommended for seismic zonation and hazard mapping in mountainous and hilly regions by regional authorities and infrastructure planners.

Keywords: seismic slope stability; sliding displacement; energy balance; earthquake wave energy; Newmark model; wave irregularity; infinite slope model; unified design diagram; arbitrary earthquakes

1. Introduction

Earthquake-induced slope displacements are commonly evaluated in engineering practice using the Newmark slope model, originally proposed by Newmark [1]. In this model, a rigid soil block above a predefined potential slip plane is subjected to a design acceleration motion, and the driving force is compared with the corresponding resistance along the slip plane (Sarma [2], Crespellani et al. [3]).

Alternatively, local accelerations within a deformable soil slope—obtained from decoupled finite element method (FEM) dynamic response analyses that account for seismic amplification—are used to calculate the global driving force. This force is then compared with the shear resistance along the slip plane (Makdisi & Seed [4], Watanabe et al. [5]). If the safety factor (defined as resistance divided by driving force) falls below unity during a given time interval of an earthquake motion, the sliding displacement is computed using the Newmark slope sliding algorithm (e.g., Kokusho [6]). Furthermore, while seismic amplification and sliding displacement are often evaluated separately in decoupled analyses, coupled evaluations have also been developed and applied to case studies (Kramer & Smith [7], Rathje & Bray [8]).

While the Newmark method was initially started from straight slip planes, circular slip planes are frequently adopted in the current practice of civil engineering design, wherein the driving

 doi:10.20944/preprints202603.1883.v1

moment about the circle center is compared to the resisting moment along the circular plane. Both of them share the basic equation of force equilibrium, though resulting displacements are typically limited to a few meters in the circular planes.

In contrast, strong earthquakes have repeatedly triggered long-distance failures in natural slopes, causing catastrophic damage. Massive debris flows have traveled considerable distances, impacting residential areas, infrastructures and river flows. To evaluate such devastating failures, Kokusho and Ishizawa [9] developed an energy-based approach using shaking table model tests, replacing force equilibriums with energy balance principles. A key finding of this approach was that slope sliding displacements δ are uniquely formulated with earthquake wave energies E_{eq} directed toward slope sliding, regardless of the input motion characteristics. Numerous case histories of slope failures during recent earthquakes have been back-analyzed using this formula to understand failure mechanisms and quantify mobilized friction coefficients.

Building on this, the "Energy-Based (EB) Newmark Method" was developed by Kokusho et al. [10]. This method couples the Newmark-type slope model with an underlying horizontal layer where SH-harmonic waves propagate to directly evaluate slope displacements δ from upward wave energy E_u. However, the application of the method has been limited so far within harmonic motions and cannot be extended to irregular waves of arbitrary earthquakes for practicing designers.

In this study, widely-diverse ten irregular earthquake motions recorded during recent destructive events in Japan are applied with stepwise increasing amplitudes to an infinitely long slope to calculate E_{eq} from the input wave energies E_u. The relationship between E_{eq} and E_u is then modified to construct a unified diagram, enabling E_{eq} to be estimated from E_u using wave and slope parameters for arbitrary earthquake motions. This allows slope displacements δ to be determined directly from E_{eq} based on a basic energy balance without resorting to conventional Newmark calculations.

2. Energy Principles for Slope Sliding

The energy balance governing earthquake-induced slope failures was first formulated by Kokusho and Kabasawa [11] as:

$$E_{gr} + E_{eq} = E_{dp} + E_k \tag{1}$$

where: E_{gr}=gravitational energy variation due to slope sliding, E_{eq}=earthquake energy contributing to sliding, E_{dp}= energy dissipated in the slide block during sliding, and E_k=kinetic energy of the slide block during sliding. All energies are defined per unit horizontal area of the slip plane. If the energy balance is considered before and after sliding (i.e., E_k =0), Eq. (1) simplifies to:

$$E_{gr} + E_{eq} = E_{dp} \tag{2}$$

In a Newmark-type sliding block model (Figure 1(a)), with friction angle ϕ, slope angle θ, and residual horizontal displacement δ, the gravitational and dissipated energies can be expressed [8] as:

$$E_{gr} = \rho g D \delta \tan\theta \tag{3}$$

$$E_{dp} = \rho g D \delta \tan\phi \left(1 + \tan^2\theta\right) \Big/ (1 + \tan\theta \tan\phi) \tag{4}$$

where ρ=density of the sliding block，g=acceleration of gravity, and D=thickness of the sliding block. Substituting into Eq. (2), the earthquake energy contributing to slope sliding becomes:

$$E_{eq} = E_{dp} - E_{gr} = \rho g D \delta \tan(\phi - \theta) \tag{5}$$

Thus, the residual displacement δ can be expressed directly from the energy balance:

 doi:10.20944/preprints202603.1883.v1

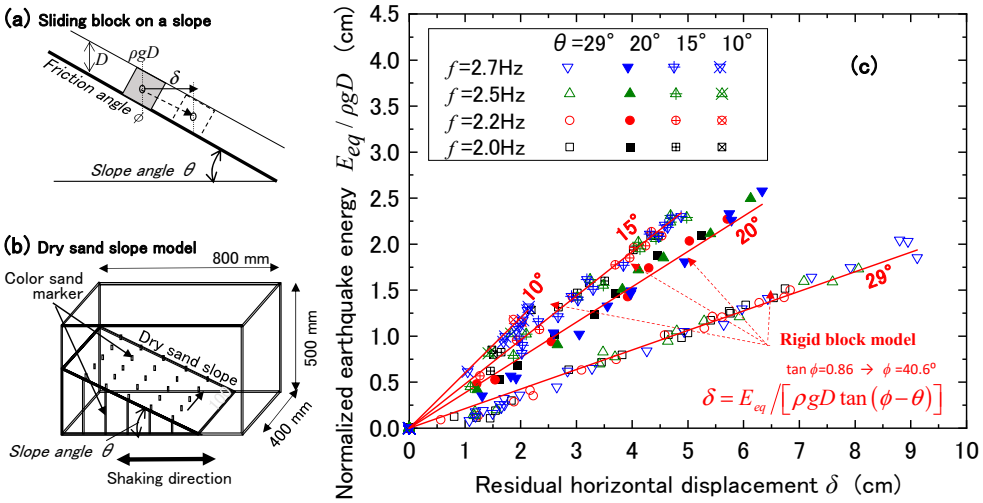

Figure 1. (a) Sliding block on a rigid slope, (b) Shaking table model test of dry sand slope, and (c) Earthquake energy versus residual displacement obtained from shaking table model tests (b) compared with theoretical equation of sliding block on rigid slope (a).

$$\delta = E_{eq} \Big/ \left[\rho g D \tan\left(\phi - \theta\right) \right] \tag{6}$$

which is central to the energy-based approach.

This equation was validated through shaking table tests (Figure 1(b)), in which dry sand slopes of varying angles were subjected to sinusoidal vibrations of different frequencies. Detailed descriptions of the test setup, energy measurements, and displacement evaluations are provided by [8]. In Figure 1(c), normalized earthquake energies $E_{eq}/\rho gD$ are plotted against average slope displacements δ for slope angles of 29°, 20°, 15°, and 10°. These test results are compared with straight lines derived from Eq. (6), using an adjusted friction angle of ϕ=40.6º. Remarkably, the simple energy theory of a rigid block on a straight slope (Figure 1(a)) reproduces the observed displacements across all slope angles and input frequencies, provided that a suitable friction angle ϕ is prescribed. This suggests that more realistic failure modes, including continuous shear deformation, can be effectively captured by the energy-based model employing the rigid slip plane.

The effectiveness of this approach was further demonstrated by applying Eq. (6) to numerous large-scale slope failures during strong earthquakes in Japan. These back-analyses enabled estimation of mobilized friction angles and provided insights into the actual failure mechanisms [9,10]. It is worth noting that the Newmark slope model shares the same fundamental mechanism as the energy-based model in Figure 1(a), assuming a rigid slip plane. Therefore, the Newmark model, when integrated with energy principles and appropriate friction coefficients, may serve as a practical tool for evaluating slope displacements in realistic shear failure modes.

3. Outline of Eb-Newmwrk Method

In Figure 2(a), the conventional Newmark model (CNM) is illustrated as an infinitely long rigid slope of friction angle ϕ and slope angle θ overlain by a sliding block of vertical thickness D and density ρ. Herein, the friction coefficient of the slope is represented solely as $\tan\phi$ using the friction angle ϕ to make the following analysis simpler, wherein the effect of cohesion c may be implicitly considered by reevaluating ϕ as $\tan^{-1}\left(\tan\phi + c/\sigma_v\right) \rightarrow \phi$ assuming constant overburden stress σ_v.

 doi:10.20944/preprints202603.1883.v1

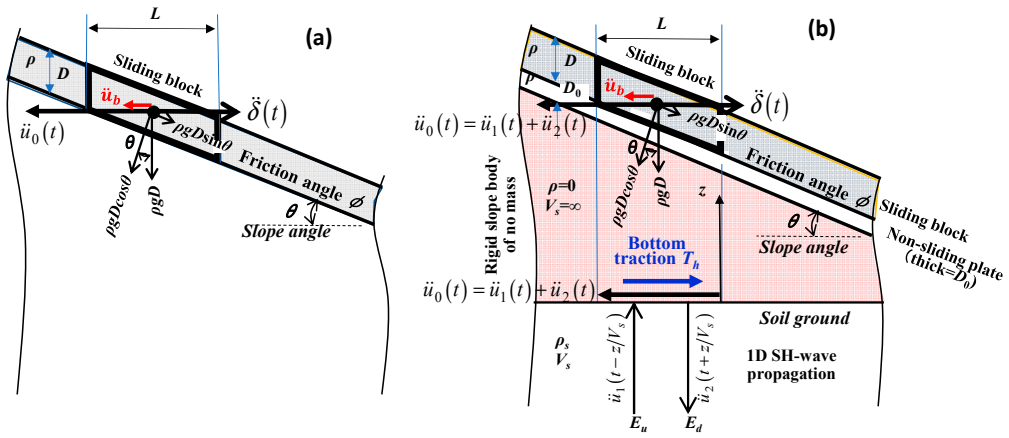

Figure 2. Slope sliding models used in this paper: (a) Conventional Newmark Model, (b) Energy-Based Newmark Model.

If the acceleration working on the slope $\ddot{u}_0$ exceeds the yield acceleration in the CNM, $g\tan(\phi-\theta)$, in the downslope direction;

$$\ddot{u}_0 - g\tan(\phi-\theta) > 0 \tag{7}$$

then, the block starts sliding with the relative acceleration $\ddot{\delta}$ as;

$$\ddot{\delta} = \left[\ddot{u}_0 - g\tan(\phi-\theta)\right]\cos(\phi-\theta)\frac{\cos\theta}{\cos\phi} \tag{8}$$

In Figure 2(b), the Energy-Based Newmark Method (EBNM) is illustrated, wherein the most pronounced difference from the CNM is how to give an input acceleration to the slope. A virtual slope body is brought in as shaded in the figure beneath the sliding block in contact with a horizontal ground underneath, where the SH-wave input motion is coming up. The horizontal wave displacement $u(t,z)$ in the soil layer of S-wave velocity V_s for time t and vertical coordinate z (upward plus) can be written as;

$$u(t,z) = u_1(t - z/V_s) + u_2(t + z/V_s) \tag{9}$$

where u_1 and u_2 stand for horizontal displacements of upward and downward SH-waves, respectively. Hence, the acceleration at the top of the soil ground z=0 is;

$$\ddot{u}(t,0) \equiv \ddot{u}_0(t) = \ddot{u}_1(t) + \ddot{u}_2(t) \tag{10}$$

This acceleration $\ddot{u}_0(t)$ transmits directly to the slope surface through the slope body, which is virtually of infinite rigidity and no mass without any wave amplification, and vibrates the sliding block in the same way as in the CNM.

Needless to say, Figure 2(b) is not a rigorous model replicating the wave propagation in two-dimensional sloping ground but a simplification from an engineering point of view. However, it may be justified for practical purposes because the CNM in Figure 2(a), too, seems to involve implicitly a similar simplification wherein horizontal ground acceleration is loaded directly on the sliding slope mass. Also note that local wave amplification due to slope geometry is not taken into account here. This is because higher frequency motions, which amplify in localized slope geometries, may be neglected in calculating slope slide displacements, which are overwhelmingly dominated by lower frequency waves, as addressed later.

The model in Figure 2(b) is further modified so that a thin non-sliding plate (thickness D_0, density ρ) is inserted beneath the sliding plane of friction angle ϕ, and glued to the top of the virtual slope body for the purpose of stabilizing the numerical integration in a time-domain dynamic response analysis, as will be explained later.

 doi:10.20944/preprints202603.1883.v1

It is readily understandable in Figure 2(b) that the energy E_{eq} dissipated in slope sliding can be equated with the difference between upward and downward energy, E_u and E_d, respectively, as;

$$E_{eq} = E_u - E_d \tag{11}$$

if the seismic energy is postulated to flow exclusively by vertically traveling SH-wave in the horizontal layer. Here, E_u and E_d are calculated from corresponding upward and downward velocity motions $\dot{u}_1(t)$ and $\dot{u}_2(t)$, one-directionally propagating SH-waves, respectively, for time interval t=0~T of a particular earthquake motion (e.g., Sarma [13]) as;

$$\begin{aligned} E_u &= \rho_s V_s \int_0^T \left| \left[\dot{u}_1(t) \right]^2 \right| dt \\ E_d &= \rho_s V_s \int_0^T \left| \left[\dot{u}_2(t) \right]^2 \right| dt \end{aligned} \tag{12}$$

The force-equilibrium of the slope model shown in Figure 2(b) can then be formulated as;

$$\rho D\left(\ddot{u}_0 - \ddot{\delta}\right) + \rho D_0 \ddot{u}_0 + \rho_s V_s^{\,2} \left.\frac{\partial u}{\partial z}\right|_{z=0} = 0 \tag{13}$$

where the first and second terms are the inertia force of the sliding block and the non-sliding plate, respectively. The third term is the seismic shear stress working at the bottom of the virtual slope body. Then it becomes;

$$\left[\rho D\left(\ddot{u}_1(t) + \ddot{u}_2(t) - \ddot{\delta}(t)\right)\right] + \left[\rho D_0\left(\ddot{u}_1(t) + \ddot{u}_2(t)\right)\right] = \rho_s V_s \left[\dot{u}_1(t) - \dot{u}_2(t)\right] \tag{14}$$

If the slope starts sliding due to increasing acceleration, Eq. (14), coupled with Eq. (7) & (8), is transformed to Eq. (15) using constants A and B defined in Eq. (16).

$$\rho D\left\{\ddot{u}_1(t) + \ddot{u}_2(t) - \left[\ddot{u}_1(t) + \ddot{u}_2(t) + B\right]A\right\} + \rho D_0\left(\ddot{u}_1(t) + \ddot{u}_2(t)\right) = \rho_s V_s \left[\dot{u}_1(t) - \dot{u}_2(t)\right] \tag{15}$$

$$\left.\begin{aligned} \ddot{\delta}(t) &= \left[\ddot{u}_1(t) + \ddot{u}_2(t) + B\right]A \\ A &= \cos(\phi - \theta)\cos\theta / \cos\phi \\ B &= -g\tan(\phi - \theta) \end{aligned}\right\} \tag{16}$$

Eqs. (15) & (16) are further simplified as Eqs. (17) & (18) by introducing another constant M as follows.

$$M\left[\ddot{u}_1(t) + \ddot{u}_2(t)\right] = \rho_s V_s \left[\dot{u}_1(t) - \dot{u}_2(t)\right] + \rho DAB \tag{17}$$

$$M = \rho D\left[1 - A + \left(D_0/D\right)\right] \tag{18}$$

Considering that A defined in Eq. (16) takes 1.0~1.1 for plausible design values as $\phi - \theta$=0～35° and ϕ=35° in ordinary slope problems, M is destined to be negative if D_0=0 (the non-sliding plate is absent). This is why the thin plate was added in the model to create the term including D_0 so that Eq. (17) can be time-integrated using the Newmark β-method with stability (Kokusho et al. [11]). However, the thickness D_0 of the non-sliding plate, virtually introduced solely for the sake of numerical stability, should be as small as possible to avoid its unfavorable effect. D_0/D=0.12 has been chosen in Eq. (18) by trial calculations so that D_0 is as near to zero as possible and M is still positive.

A series of finite difference calculations of the EB-Newmark model in Figure 2(b) have been conducted for harmonic input motions utilizing Eqs. (17) and (18) for infinitely long slopes of ϕ=35°, $\phi - \theta$=5, 10, 15°, ρ=ρ_s=1.8 t/m³, V_s=200 m/s, where harmonic motion f=1.0 Hz is given with stepwise increasing amplitudes A_1 [11]. In Figure 3, the earthquake energies E_{eq}=E_u−E_d are plotted versus residual displacements δ of the sliding block. The calculated E_{eq} and δ are all evaluated as stationary values per one cycle. Three dashed lines in the chart representing the theoretical Eq. (6) are in perfect agreement with the computed plots, indicating that the energy balance theory expressed in Eqs. (1) to (6) is replicated exactly by the Newmark calculation. Also note that the above-mentioned

 doi:10.20944/preprints202603.1883.v1

modification of the model with the additional non-sliding plate of D_0/D=0.12 for numerical stability performs very well without any detrimental effects.

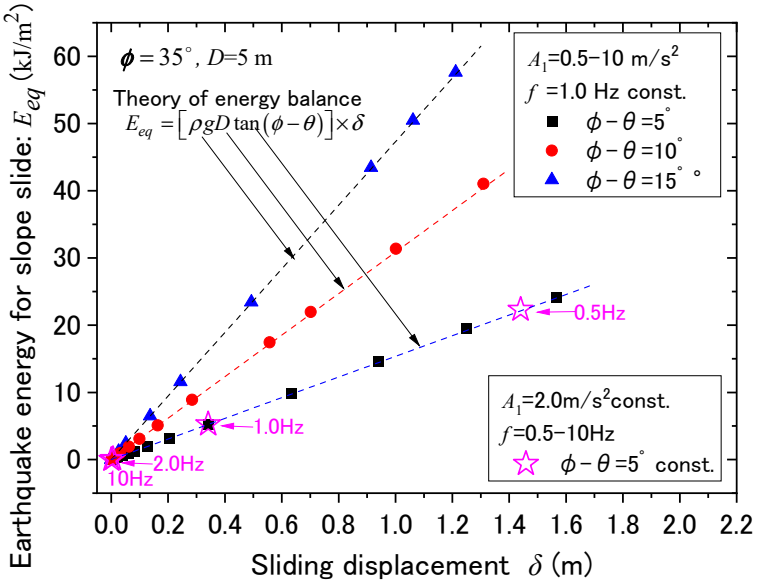

Figure 3. Earthquake energies for slope slide E_{eq} versus slide displacements δ of sliding blocks calculated by EBNM for varying acceleration amplitudes A_1 and frequencies f, compared with theoretical equation.

Furthermore, the star symbols in Figure 3, representing $\phi - \theta$=5° and constant acceleration amplitude A_1=2.0 m/s^2 while the input frequency is varied f=0.5~10Hz stepwise, indicate that the energy theory in Eq. (6) is universally applicable in evaluating slope displacements despite widely different input frequencies. In contrast, the acceleration A_1 cannot serve as a unique parameter, obviously, because the same acceleration 2.0 m/s^2 results in widely separated displacements δ due to the difference in frequency f. The above finding highlights how effective the energy concept is in evaluating slope displacements, as already demonstrated by a series of shaking table tests of model slopes [8], in contrast to the acceleration used in current practice.

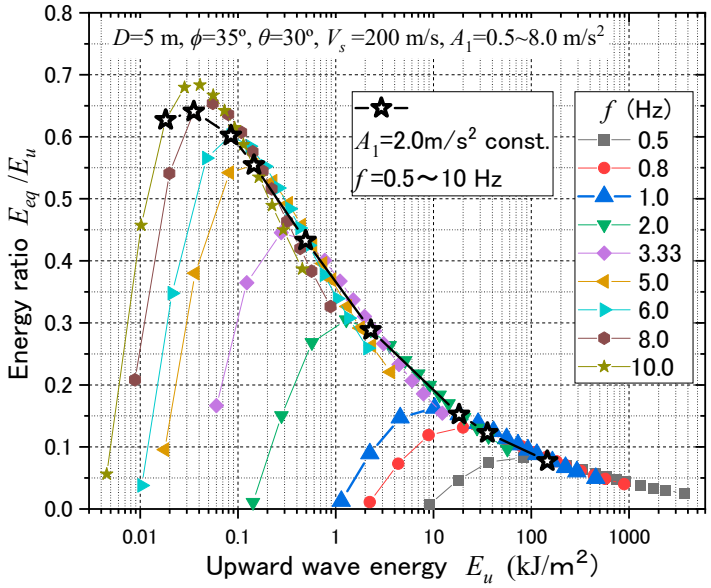

Figure 4. Energy ratio E_{eq} / E_u, versus upward wave energy E_u calculated for a slope of D=5 m, ϕ=35º, θ=30º, for harmonic waves with constant acceleration amplitude A_1=2.0 m/s^2 and variable frequency f=0.5~10 Hz.

 doi:10.20944/preprints202603.1883.v1

In Figure 4, the energy ratios E_{eq}/E_u calculated for harmonic waves of frequency f=0.5 to 10 Hz are plotted on the vertical axis versus E_u in the horizontal log axis corresponding to stepwise-increasing wave amplitudes. While E_{eq} simply increases with increasing E_u, E_{eq}/E_u shows a clear peak followed by a monotonic decline with increasing E_u, because the increment rate of E_{eq} to E_u tends to decrease in the midst of the E_{eq}~E_u relationship. Quite remarkably, the E_{eq}/E_u ~ E_u curves are very similar to each other, while the peak values $(E_{eq}/E_u)_{peak}$ tend to be greater and occur at lower E_u as corresponding frequencies f of the harmonic motions are getting higher. This implies that there exists an optimum frequency f wherein the earthquake energy E_u is most efficiently directed to the energy E_{eq} for slope sliding.

In Figure 5, the energy E_u, E_{eq}, and the ratio E_{eq}/E_u in a single cycle of a harmonic wave of constant acceleration amplitude A_1=2.0 m/s² are plotted against f=0.5~10.0 Hz. E_u tends to decrease drastically in inverse proportion to the cube of f under a constant A_1, as implied in Eq. (12). Accordingly, E_{eq} tends to decrease significantly with f compared to E_{eq} 100% at f =1 Hz, down to 21% at f =2 Hz, 6% at f =3.3 Hz, and 2% at f =5 Hz. Considering that the slide displacement δ is directly proportional to E_{eq} in Eq. (6), high-frequency motions for $f \geq 3 \sim 4$ Hz are almost ignorable in calculating slope slide displacements, as already stated before. In the same graph, the energy ratio E_{eq}/E_u calculated for A_1=2.0 m/s² constant is plotted with open triangular symbols against f. The same ratio E_{eq}/E_u is plotted versus E_u with star symbols in Figure 4 to compare with the E_{eq}/E_u versus E_u plots calculated for parametrically changing frequencies. This indicates that the E_{eq}/E_u-values in Figure 5 are almost coincidental with the peak values $(E_{eq}/E_u)_{peak}$ for f=0.5~9.0 Hz in Figure 4. As for E_{eq}/E_u, a considerable surge of about 10 times is observed with increasing f from 0.5 to 10 Hz in Figure 5. However, if E_{eq}/E_u is normalized as $(E_{eq}/E_u)/(\alpha\beta)$, it becomes almost f-insensitive within ±6% difference from the average over f=0.5~10 Hz, as indicated with triangles connected with a thick curve. Here, constants α and β are functions of the slope parameters, ρ, ρ_s, D, V_s, and f-dependent as formulated in Eqs. (19) and (20), and also indicated in Figure 5.

$$\alpha = (2\pi f \rho D)/(\rho_s V_s) \tag{19}$$

$$\beta = [1 - Df/V_s]^3 \tag{20}$$

This normalization serves as a key to develop a unified diagram of energy-based evaluation on slope slide displacements δ directly from the upward wave energies E_u for not only harmonic but also irregular earthquake waves in the next sections.

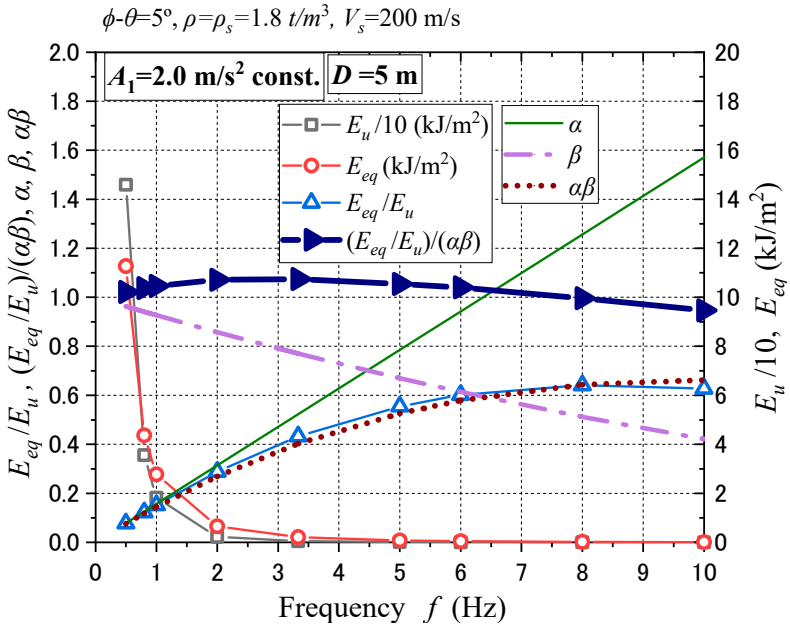

 doi:10.20944/preprints202603.1883.v1

Figure 5. Energy ratio E_{eq}/E_u, normalized energy ratio $(E_{eq}/E_u)/(\alpha\beta)$, E_u, E_{eq}, α, β, and $\alpha\beta$ versus frequency f calculated for a slope of D=5 m, ϕ=35º, θ=30º, by harmonic waves of constant acceleration A_1=2.0 m/s² and frequency f=0.5~10 Hz.

4. Eb-Newmark Analysis Using Ten Diverse Earthquake Records

Ten earthquake ground motion records, designated Wv. 1 through Wv. 10 and summarized in Table 1, were selected for EB-Newmark slope sliding analysis. These records originate from destructive seismic events that occurred in Japan over the past three decades, representing a wide range of characteristics: moment magnitudes M_J from 6.7 to 8.0 (Japan Meteorological Agency scale, approximately equivalent to surface magnitude M_s), hypocenter distances R from 9 to 117 km, and peak ground accelerations (PGA) ranging from 2.5 to 24.5 m/s².

All acceleration records were processed using a band-pass filter (BPF) with the period band of 0.1–5 s. The portion of each record used in the analysis spans from the onset of the SH wave to the final point where residual acceleration falls within 4–8% of the peak. Figure 6 presents the velocity response spectra, which capture long-period motions critical to slope failure better than acceleration spectra. The spectral peak periods of the records range from 0.2 to 2.0 s and can be categorized into two groups: Group 1 (Wv.1, Wv.6 ~ Wv.10) with isolated sharp peaks, and Group 2 (Wv.2 ~ Wv.5) with broad, multi-spectral dull peaks. Slope parameters used in the analysis are consistent with those applied to harmonic wave cases: friction angle ϕ=35°, inclination angle difference $\phi-\theta$=5°, sliding depth D=5 m, initial displacement ratio D_0/D=0.12, unit weight $\rho=\rho_s$=1.8 t/m³, and shear wave velocity V_s=200 m/s.

Figure 7 illustrates the relationship between sliding displacement δ and input energies E_u or E_{eq} on a log-log scale. For individual earthquakes, input amplitudes were scaled incrementally, and results are plotted using line-connected symbols. While δ–E_u plots (solid symbols) vary significantly across the earthquakes, δ–E_{eq} plots (open symbols) are unified, aligning closely with the theoretical expression given in Eq. (6). This highlights the unique role of E_{eq} in governing δ, independent of wide differences in amplitude, frequency content, irregularity, or duration. To leverage this uniqueness, however, E_{eq} or the ratio E_{eq}/E_u must be evaluated from E_u.

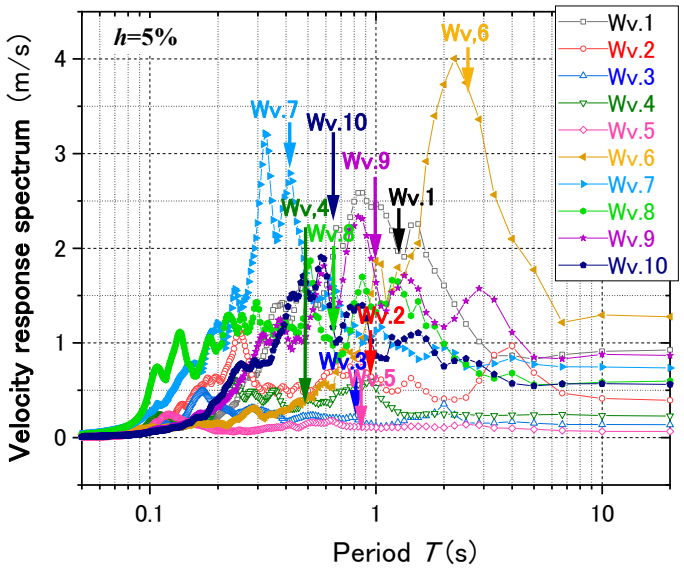

Figure 6. Velocity response spectra (h=5%) of ten earthquake records compared with equivalent predominant periods T^* derived from $(E_{eq}/E_u)_{peak}\sim f$ curve of harmonic waves.

 doi:10.20944/preprints202603.1883.v1

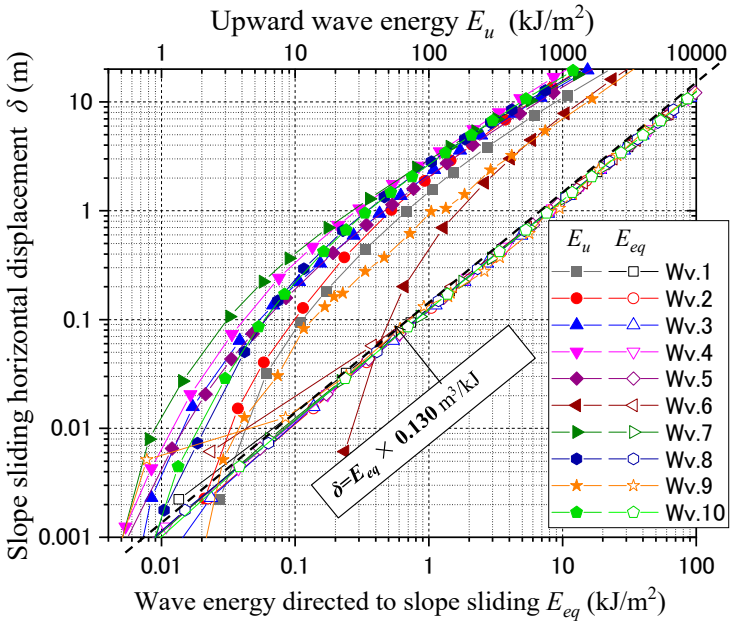

Figure 7. Slope sliding displacement δ versus upward energies E_u or energies E_{eq} directed to slope sliding calculated by EBNM for ten earthquakes.

Figure 8(a) shows the semi-log plot of E_{eq}/E_u versus E_u for the ten records. Star symbols represent analogous results for harmonic motion at f=1.0 Hz (see Figure 4). The E_{eq}/E_u–E_u curves for earthquake records resemble those of harmonic waves: rising from zero, peaking, and then declining. The peak values of E_{eq}/E_u range from 0.06 to 0.33, with higher peaks occurring at lower E_u-values, a trend also observed in Figure 4 for harmonic cases, where frequency plays a key role.

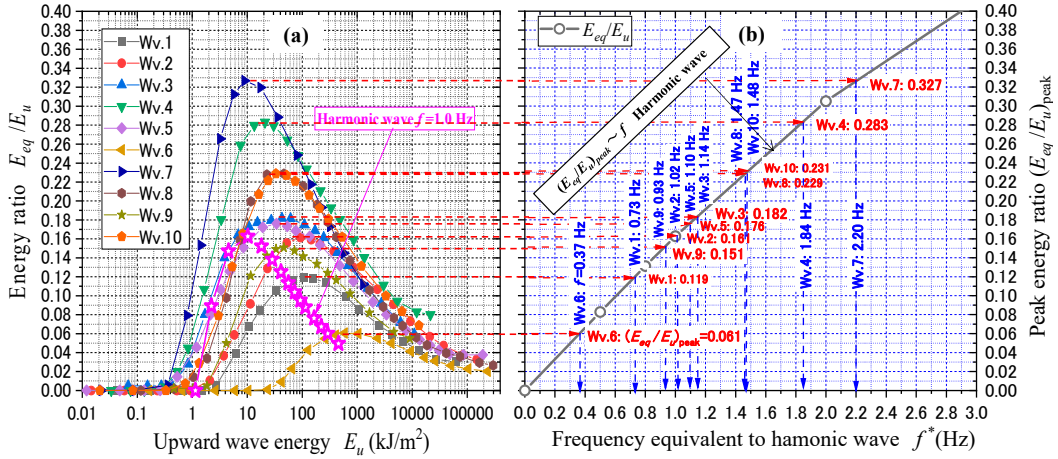

Figure 8. (a) $E_{eq}/E_u \sim E_u$ correlations of 10 earthquakes, and (b) $(E_{eq}/E_u)_{peak} \sim f$ curves of harmonic wave where equivalent frequencies f^* are read off.

To explore this frequency dependency, the peak E_{eq}/E_u-values from Figure 8(a) are compared in Figure 8(b) with a reference curve, which is drawn by combining the peaks of E_{eq}/E_u for harmonic motions of different frequencies f in Figure 4. By projecting each peak in Figure 8(a) horizontally to the reference curve in Figure 8(b), equivalent harmonic frequencies f^* are read off in Figure 8(b) corresponding to individual earthquake records. These f^*-values and corresponding periods T^*=1/f^* are listed in Table 1 and also indicated with arrows in the velocity spectra of Figure 6. The periods thus obtained are mostly consistent with the spectral peaks, though exact matches are difficult,

 doi:10.20944/preprints202603.1883.v1

suggesting that $E_{eq}/E_u \sim E_u$ in irregular records mimics the frequency-dependent trends of harmonic waves.

In Figure 5, the E_{eq}/E_u-ratio for harmonic waves was normalized using parameters α and β in Eq. (19) & (20) to yield a frequency-insensitive metric: $(E_{eq}/E_u)/(\alpha\beta)$. The same normalization applied to the E_{eq}/E_u-ratio calculated for the earthquake waves using their respective equivalent frequencies f^* yields the vertical coordinates $(E_{eq}/E_u)/(\alpha\beta)$ in Figure 9, where the peak values are nearly identical across the ten waves with mean ± SD = 1.10 ± 0.014, confirming the effectiveness of this normalization.

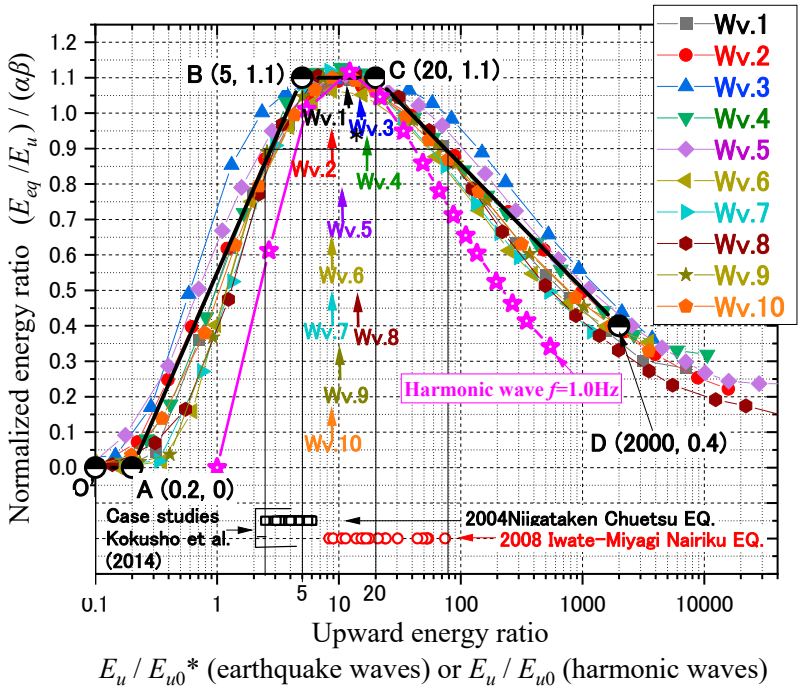

Figure 9. Normalized energy ratio $(E_{eq}/E_u)/(\alpha\beta)$ versus upward energy ratio E_u/E_{u0}^* calculated by EBNM for ten earthquakes, approximated by a broken line OABCD.

To normalize the horizontal axis, too, reference energies E_{u0}^* are introduced such that $(E_{eq}/E_u)/(\alpha\beta) \sim E_u/E_{u0}^*$ curves are unified as closely as possible with the harmonic wave of f = 1.0 Hz. The E_{u0}^* values thus optimized are plotted against the equivalent frequencies f^* in Figure 10 (open squares), forming a regression curve with $R^2 = 0.90$.

$$E_{u0}{}^* = 5.66\times(f^*)^{-2.14} \tag{21}$$

For comparison, E_{u0}-values, yield energies for harmonic waves [11] calculated from Eq. (12) corresponding to yield acceleration $g\tan(\phi-\theta)$ are also plotted (the dashed line).

$$E_{u0} = \rho_s V_s g^2 \Big/ \left(32\pi^2 f^3\right) \times \tan^2(\phi-\theta) = 0.838\times(f)^{-3.00} \tag{22}$$

Although E_{u0}^* lacks a logical definition due to the randomness of earthquake motions, its similarity to E_{u0} in monotonically decreasing with increasing frequency as a power function suggests a similar role in triggering slope failure.

The normalized plots in Figure 9 reveal a unified pattern across all earthquake waves: a plateau near $E_u/E_{u0}^* \approx 10$, flanked by ascending and descending slopes. Compared to harmonic waves, earthquake records exhibit gentler slopes and broader plateaus, especially for Wv.3 and Wv.5, which have flat spectra (Figure 6). This is likely due to E_{u0}^* reflecting a spectrum of multiple peaks rather than a single peak. In harmonic cases, sliding initiates at $E_u/E_{u0} = 1.0$ [11], consistent with the yield energy definition in Eq. (22). For earthquake records, sliding tends to begin at $E_u/E_{u0}^* \approx 0.1$–0.4, reflecting the lack of a clear yield threshold. Despite these differences, the normalized chart in Figure 9 successfully integrates the diverse $E_{eq}/E_u - E_u/E_{u0}^*$ relationships from Figure 8(a).

 doi:10.20944/preprints202603.1883.v1

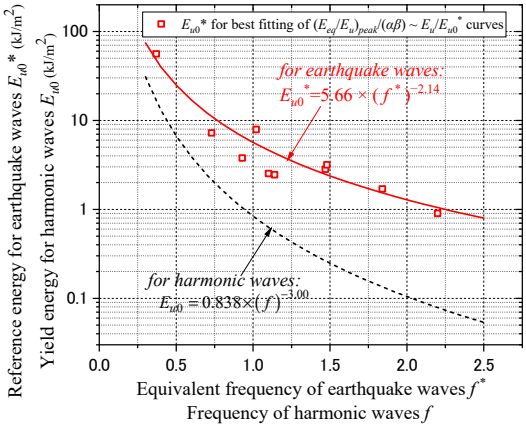

Figure 10. Reference energy E_{u0}^* versus equivalent frequency f* for earthquake waves compared with yield energy E_{u0} versus f for harmonic waves.

To assess parameter sensitivity, additional analyses are performed using Wv.10, varying ϕ–θ, D, and V_s. In Figure 11(a), varying ϕ–θ from 2.5° to 15° yields consistent normalized curves, as both vertical and horizontal axes adjust accordingly. In Figure 11(b), increasing D beyond 8 m introduces deviations: ~10% error in E_{eq} for D= 10 m and ~20% for D= 20 m. However, this is not critical, as E_{eq} is typically much smaller than gravitational energy E_{gr} in thick large-scale slides [9], leading to the evaluation error in E_{eq} being less significant in the energy balance in Eq. (2). In Figure 11(c), variations in V_s have a negligible impact on the normalized correlation.

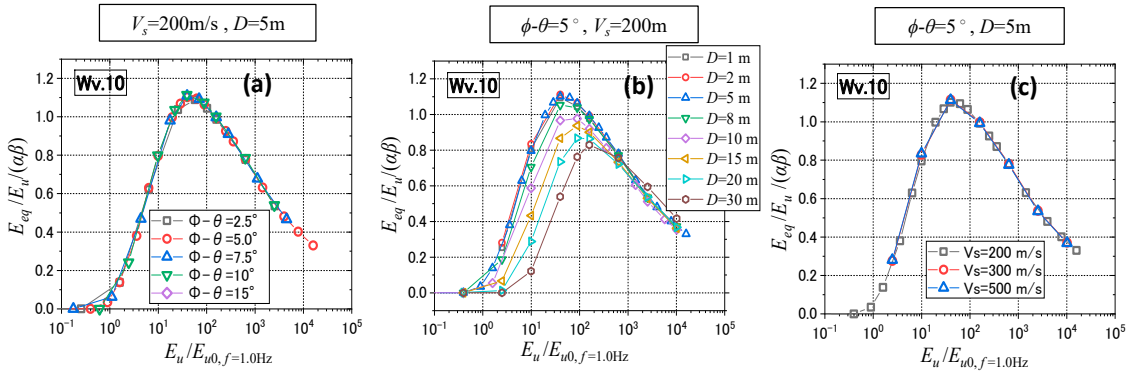

($E_{u0,f=1\ Hz}$=0.838 kJ/m^2):

Figure 11. $E_{eq}/E_u \sim E_u/E_{u0,f=1\ Hz}$ plots calculated for Wv. 10 for a variety of parameters: (a) ϕ–θ =2.5~15º, (b) D=1~30 m, (c) V_s=200~500 m/s.

5. Unified Slope Slide Evaluation for Arbitrary Motions

The correlation between $(E_{eq}/E_u)/(\alpha\beta)$ and E_u/E_{u0}^*, as shown in Figure 9, provides a convenient framework for evaluating E_{eq} directly from E_u. These nearly unified curves for ten earthquake records can be approximated by a set of broken lines (OABCD) on a semi-logarithmic graph and formulated in Eq. (23):

$$\left.\begin{array}{lll} \text{OA}: & E_u/E_{u0}^* \le 0.2 & E_{eq}/E_u/(\alpha\beta) = 0 \\ \text{AB}: & 0.2 < E_u/E_{u0}^* \le 5.0 & E_{eq}/E_u/(\alpha\beta) = 1.58 \cdot \log_{10}\left(E_u/E_{u0}^*\right) \\ \text{BC}: & 5.0 < E_u/E_{u0}^* \le 20 & E_{eq}/E_u/(\alpha\beta) = 1.10 \\ \text{CD}: & 20 < E_u/E_{u0}^* \le 2000 & E_{eq}/E_u/(\alpha\beta) = -0.35 \cdot \log_{10}\left(E_u/E_{u0}^*\right) + 1.56 \end{array}\right\} \quad (23)$$

 doi:10.20944/preprints202603.1883.v1

Using this formulation, steps to evaluate slope sliding energy E_{eq} and displacement δ for arbitrary design earthquakes are as follows:

(1) If design acceleration waves $\ddot{u}_0(t)$ in Eq. 10 are available for direct input to slopes, the upward SH-waves may be approximated as $\ddot{u}_1(t) = \ddot{u}_0(t)/2$ by assuming complete reflection at the soil surface. The upward energy E_u can then be calculated from Eq. (12) using upward velocity waves, $\dot{u}_1(t) = \int \ddot{u}_1(t)dt$, and the predominant frequency f_p is determined from the response spectrum of $\dot{u}_1(t)$.

(2) If design motions are unavailable, begin by selecting the earthquake magnitude M and hypocenter distance R (in meters). The input wave energy E_{ip} (in kJ/m^2) at bedrock can be roughly estimated using energy radiation principles and the empirical formula by Gutenberg [14], as presented by Kokusho and Suzuki [15]:

$$E_{ip} = E_0 \Big/ \left(4\pi R^2\right) \tag{24}$$

$$\log E_0 = 1.5M + 1.8 \tag{25}$$

For greater accuracy, fault and path mechanisms should be considered. The predominant frequency f_p, inversely correlated with M (*e.g.*, Aki [16]), may be predicted using regional earthquake databases. The upward energy E_u for a specific slope is then determined from E_{ip} using the S-wave impedance ratio between the layer beneath the slope and the bedrock $\rho_s V_s / \rho_{sb} V_{sb}$ as:

$$E_u = E_{ip} \times \left(\rho_s V_s / \rho_{sb} V_{sb}\right)^{0.7} / 2 \tag{26}$$

This empirical relation, developed by Kokusho & Suzuki [15], is based on numerous strong motion records from vertical arrays. The division by 2 in the equation accounts for the average contribution of horizontal SH-wave energy in the sliding direction.

(3) The reference energy E_{u0}^* is calculated from Eq. (21) by substituting the peak frequency f_p into the equivalent frequency f^*. Slope parameters θ, ϕ, V_s, ρ, and D are then used to compute α and β in Eqs. (19) and (20). With the horizontal coordinate E_u/E_{u0}^*, the vertical coordinate $(E_{eq}/E_u)/(\alpha\beta)$ is read off from Figure 9 or calculated using Eq. (23). For $E_u/E_{u0}^* < 0.2$, where $E_{eq}/E_u = 0$, slopes may be considered stable, though minor variability may exist. Otherwise, a positive E_{eq} leads to a non-zero displacement δ, which is readily obtained from Eq. (6).

In Figure 9, the vertical coordinate $(E_{eq}/E_u)/(\alpha\beta)$ ranges from 0 to 1.10 as the horizontal coordinate E_u/E_{u0}^* spans from approximately 0.2 to over 1000. This indicates that the energy directed toward slope sliding varies significantly with upward energy. The ten earthquake records in Table 1 used here are all strong motions obtained in damaged areas, some including actual slope failures. Arrows in Figure 9 mark the normalized upward energies E_u/E_{u0}^* all falling between 5 and 20 for Wv. 1 to Wv. 10 within the plateau region BC, suggesting that typical strong motions in Japan tended so far to yield $(E_{eq}/E_u)/(\alpha\beta) = 1.10$.

Among the ten events, the 2004 Niigataken Chuetsu and 2008 Iwate-Miyagi Nairiku earthquakes triggered numerous slope failures in mountainous terrains. Case studies on affected slopes during the events exhibited runout distances ranging from a few to over 100 meters [14,17]. The corresponding E_u/E_{u0}^* values for these slopes plotted with two-type open dots at the bottom of Figure 9 range from 2.5 to 80, yielding the $(E_{eq}/E_u)/(\alpha\beta)$-values between 0.90 and 1.10. Hence, this range seems to be representative in field observations and aerial imagery during the two events. According to Figure 9, slope sliding initiates at $E_u/E_{u0}^* = 0.2$, where E_{eq} and δ start to be positive. The gap between 0.2 and 2.5 may be considered as a transition zone where minor cracking evolves into measurable displacements.

In summary, the EB-Newmark method offers a significant benefit for risk analysis of earthquake-induced slope failures in hilly and mountainous regions. Though, slopes in practice are sometimes approximated by circular slope models, the infinitely long straight slope condition assumed here may fit to natural slopes better because of intrinsic geological structures and suit to zonation studies on co-seismic slope sliding covering wider regions. Unlike the CNM, it does not require time-domain

 doi:10.20944/preprints202603.1883.v1

acceleration inputs for each slope. Instead, it accommodates diverse slope gradients, shear strengths, and earthquake scenarios through parametic variations. Hence, it is well-suited for probabilistic risk assessments, seismic zonation studies by local governments, and infrastructure screening for roads, railways, and utility pipelines traversing mountainous terrains.

6. Summary

The Energy-Based Newmark Method (EBNM) has been applied to ten widely varied earthquake motions to evaluate slope displacements of infinitely long slopes with variable parameters. This study has led to the development of a unified methodology for estimating slope sliding displacements for arbitrary earthquake inputs without any conventional numerical calculations, yielding the following key findings:

(i) Slope displacement δ is uniquely expressed by the earthquake energy directed toward slope sliding E_{eq} using a simple formula: $\delta = E_{eq} / \left[\rho g D \tan(\phi - \theta) \right]$ where ϕ= the friction angle, θ=the slope angle, ρg=the unit weight, and D is the thickness of the sliding block. This relationship holds irrespective of acceleration, duration, or frequency content of earthquake motions. The energy E_{eq} is defined as the difference between upward and downward wave energies beneath the slope: $E_{eq}=E_u-E_d$.

(ii) Energy ratio E_{eq}/E_u tends to rise with increasing upward energy E_u from zero at the onset of sliding, reach a peak, and then decline monotonically. Despite the differences in the $E_{eq}/E_u \sim E_u$ correlations across different earthquake waves, which is found to be mainly attributable to differences in predominant frequency f_p, they basically share the same trend.

(iii) The correlations have been reformulated as $(E_{eq}/E_u)/(\alpha\beta) \sim E_u/E_{u0}^*$, where α and β are slope-dependent constants, and E_{u0}^* is a reference energy based on f_p. This unified relationship is represented by a set of broken lines (OABCD) on a design chart or by Eq. (23). Once E_u is known, E_{eq}/E_u can be obtained from the chart, and δ can be readily calculated from E_{eq} using the key formula, Eq. (6).

(iv) The upward energy E_u can be directly calculated from design acceleration motions, if available. Otherwise, it may be estimated using empirical formulas based on earthquake magnitude M and hypocenter distance R, assuming spherical energy radiation. In case histories of earthquakes, the normalized energy values E_u/E_{u0}^* for damaged slopes ranged from 2.5 to 80, corresponding to $(E_{eq}/E_u)/(\alpha\beta)$=0.9–1.1. The chart also indicates that slope sliding initiates at $E_u/E_{u0}^* \approx 0.2$. The gap between 0.2 and 2.5 may represent an energy allowance where minor fissures evolve into measurable displacements.

In conclusion, the EBNM offers significant benefits for risk analysis of earthquake-induced slope failures in hilly and mountainous terrains. Unlike the CNM, it does not require time-domain numerical analyses using acceleration inputs for individual slopes. Instead, it accommodates diverse slope conditions and earthquake scenarios by adjusting relevant parameters. The method is well-suited for probabilistic risk assessments, seismic zonation studies by local authorities, and contingency planning for infrastructure such as roads, railways, and pipelines in mountainous regions.

Nevertheless, despite its potential for simplified seismic slope stability evaluations, validation studies remain limited, though this applies to the CNM as well. To enhance the credibility of the EBNM, it is essential to accumulate and analyze case history data, comparing the observed failures with the predictions. Such efforts will help clarify the method's strengths and limitations and promote its acceptance within the engineering community.

Acknowledgments: The authors gratefully acknowledge Professor Huolang Fang of Zhejiang University, China, for his valuable suggestion to introduce the virtual term D_0 in Eq. (18), which ensures the positivity of M in Eq. (17), thereby enabling stable finite difference calculations. The authors also acknowledge the National Research

 doi:10.20944/preprints202603.1883.v1

Institute for Earth Science and Disaster Resilience (NIED), Tsukuba, and other organizations in Japan for generously disseminating their earthquake records used in this study.

Declaration of Interest: The authors declare that they have no known competing financial interests or personal relationships that could have appeared to influence the workwritten in this paper.

References

1. Newmark, N. M. (1965). Effects of earthquakes on dams and embankments, Fifth Rankine Lecture, *Geotechnique*, Vol.15, 139-159.
2. Sarma, S. K. (1975). Seismic stability of earth dams and embankments, *Geotechnique*, 25, No.4, 743-761.
3. Crespellani, T., Madiai, C. and Vannucchi, G. (1998). Earthquake destructiveness potential factor and slope stability, *Geotechnique*, 48, No.3, 411-419.
4. Makdisi, F. I. and Seed H. B. (1978). Simplified procedure for estimating dam and embankment earthquake-induced deformations, *Journal of Geotechnical Engineering*, Div. ASCE, Vol.104, No.GT7, 849-867.
5. Watanabe, H. Sato, S. and Murakami, K. (1984). Evaluation of earthquake-induced sliding in rockfill dams, *Soils and Foundations*, 24 (3), 1-14.
6. Kokusho, T. (2017). Innovative Earthquake Soil Dynamics, Chap.4, CRC publishers. Chap. Slope stability during earthquakes, 415-453.
7. Kramer, S. L., and Smith M.W. (1997). Modified Newmark model for seismic displacements of compliant slopes, *J. Geotechnical Geoenvironmental Engineering*, ASCE, 123(7), 635–644.
8. Rathje E. M. and Bray J.D. (2000). Nonlinear coupled seismic sliding analysis of earth structures", *Journal of Geotechnical and Geoenvironmental Engineering*, ASCE, 126(11), 1002–1014.
9. Kokusho, T. and Ishizawa, T. (2007). Energy approach to earthquake-induced slope failures and its implications, *Journal of Geotechnical and Geoenvironmental Engineering*, ASCE, Vol.133, No.7, 828-840.
10. Kokusho, T., Ishizawa, T. and Koizumi, K. (2011). Energy approach to seismically induced slope failure and its application to case histories, *Engineering Geology*, Elsevier, Vol. 31, 1540-1550.
11. Kokusho, T., Koyanagi, T. and Yamada, T. (2014). Energy approach to seismically induced slope failure and its application to case histories –Supplement-, *Engineering Geology*, Elsevier, Vol. 181, 290–296.
12. Kokusho T., Mori J., Mizuhara M., and Huolang F. (2022). Energy-based Newmark method for earthquake-induced slope displacements Revisited, *Soil Dynamics and Earthquake Engineering*, 162.
13. Kokusho, T. and Kabasawa, K. (2004). Slope failure evaluation by energy approach in hydraulic fill dams due to liquefaction-induced water films, Proc. 13th World Conf. on Earthquake engineering, Vancouver, Canada, Paper No. 131.
14. Sarma, S. K. (1971). Energy Flux of Strong Earthquakes, *Techtonophysics*, Elsevier Publishing Company, 159-173.
15. Gutenberg, B. (1956). The energy of earthquakes, *Quarterly Journal of the Geological Society of London*, Vol. CXII, No.455, 1-14.
16. Kokusho, T. and Suzuki, T. (2012). Energy flow in shallow depth based on vertical array records during recent strong earthquakes (Supplement), *Soil Dynamics & Earthquake Engineering*, Vol. 42, 138-142.
17. Aki. K. (1967). Scaling law of seismic spectrum, *Journal of Geophysical Research*, Vol.72, No.4. 1217-1231.
18. Kokusho, T., Ishizawa, T. and Hara, T. (2009). Slope failures during the 2004 Niigataken Chetsu earthquake in Japan, *Earthquake Geotechnical Case Histories for Performance-Based Design*, Balkema, CRC Press, 47-70.